Kinetic Monte Carlo Study of Competing Hydrogen Pathways into Connected (100), (110), and (111) Ni Surfaces

Kenneth Haug* and Gretel Raibeck

Department of Chemistry, Lafayette College, Easton, Pennsylvania 18042

Received: May 8, 2003; In Final Form: August 13, 2003

Hydrogen mobility upon and pathways into connected surfaces of a fcc metal, using the Ni (100), (110), and (111) faces as a model, are examined through computational methods. Our interest is in finding the time scale for an initial H-atom population density deposited on the surface to reach an equilibrium surface and sublayer distribution, and to understand the H dynamics in the region of Ni surface steps. The activation energies for H mobility from site-to-site are determined using a realistic potential energy function, and a set of 232 transition state theory rate constants governs the H-hopping model. A handful of the TST rate constants are compared favorably to very accurate calculations of rate constants for the same potential using a 3-d quantum mean field method. The set of TST rate constants are used in a kinetic Monte Carlo solution of the rate equations for surface hopping and surface penetration to complete the picture. We find that fast diffusion of H atoms occurs on all of the Ni surfaces with H atoms rapidly exchanging surfaces via both concave and convex step edges, and leaving the less stable (111) face. We examine the time scale for the approach to equilibrium for the H atoms on both the surfaces and sublayers. The effect of convex step edges vs the effect of direct terrace penetration for the H atoms is examined, and we find that at temperatures below about 1000 K the H-atom penetration at convex step edges becomes the favored pathway to the subsurface. As the H atoms flow via the step edges to the sublayer, a transient cycling current of H-atom probability is set up near the step edge, which fades away as equilibrium is reached.

I. Introduction

The experimental interest in growing thin, smooth metallic films has led to a theoretical effort in understanding microscopic growth and mobility mechanisms involved in metallic films.[1−30] Of additional importance in the growth process is the role impurities play in the growth mechanism, and some experimental reports have noted that impurities can help to induce the layer-by-layer growth of a metal film in some cases, or can hinder the layer-by-layer growth in other cases.[21−27] In particular, a hydrogen impurity absorbed on metal surfaces has been noted as affecting metal growth by either hindering metal adatom self-diffusion, or by enhancing it, depending on the system.[21] In some of the work that we have been involved in, experimental results were reported that H induces layer-by-layer growth of Cu(100), and similar computational predictions were noted for the closely related fcc metal Ni(100) surface.[1]

A continuation of our computational studies on Ni growth for (110) and (111) surfaces in addition to the (100) surface,[3−4] found that the presence of H on Ni(100) catalyzes the mobility of lone Ni adatoms across the surface resulting in accelerated island formation on time scales of the deposition itself. As part of the continuing interest in understanding step-dynamics and 3-d island growth,[28−30] we also examined how H atoms modified the Erlich−Schwoebel step edge barriers that govern 3-d island formation.[3] In our own earlier work,[2,4] the H-atom mobility was handled by redistribution based upon Boltzmann statistics due to the wide separation in time scale separating the H and Ni adatom mobilities, and for surface atom mobilities our test calculations confirmed that Boltzmann redistributions were

reasonable. However, it also became clear in our studies that sublayer H atoms could have a significant impact on Ni adatom mobilities.[1,4] This finding motivates our current study to better understand the transient dynamics of H-atom mobility upon and penetration into the Ni surfaces following initial surface adsorption.

The diffusion of H atoms on metal surfaces, of course, has itself a long history going back over 40 years and only partially noted in the references,[31−38] and while some of this work focused especially on the low-temperature tunneling diffusion,[36−38] the earliest work involved higher temperature activated diffusion that interests us in this study.[31,32] Much recent work is also at temperatures in the activated regime and involves hydrogen diffusion on metals, bonding to metals, and reaction from adsorbed situations.[39−45]

In this paper we report computational kinetic Monte Carlo (KMC) experiments that examine the time scale and pathways of H-atom mobility across the step edges connecting (100), (110), and (111) surfaces and also the time-scale and pathway of H-atom penetration in the sublayer of the surfaces. To carry out the KMC simulations reported here, a set of 232 rate constants for activated H-atom mobilities were calculated. In section II, we specify the surface model for the KMC study and report on the activation energy calculations that determine the rate constants within a semiclassical transition state theory (TST) approach. For a handful of cases, we have compared these approximate rate constants with more accurate ones calculated within a quantum mean field approach, as discussed in Appendix A. The KMC simulation methods are also discussed in section II, and the KMC results regarding H-atom diffusion and surface penetration patterns are examined in section III. In section IV,

---

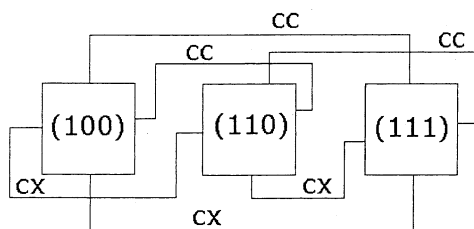* To whom correspondence should be addressed.

Figure 1. Schematic diagram of the connections among the (100), (110), and (111) surfaces used in the KMC study. The interconnections are ascending and descending step edges labeled as cc (concave) or cx (convex), respectively.

a simple kinetic model is used to illustrate one interesting feature that arises from the important convex step edge H-atom penetration: a transient cycling current of H-atom probability is maintained when the H-atom population is in a surface dominant nonequilibrium regime.

II. Theoretical Model

(a) Surface Model. The surface model for our study includes equal areas of Ni(100), (110), and (111) flat terrace surfaces connected one to another by three step-up or ascending-step intersections (we will use the term "concave-step" for clarity), and three step-down or descending-step intersections (we will use the term "convex-step" clarity).[46] Sites are labeled according to the fcc positions of Ni. Therefore on the (111) surface neighboring fcc/hcp sites are grouped as one site (using the binding energy at the fcc site for consistency), and on the (110) surface the short-axis and long-axis binding sites are grouped as one (using binding energy at the long-axis site for consistency). For notational convenience we label the three surfaces (100), (110), and (111) as, respectively, the A, B, and C surfaces. The binding energies upon and the rate constants for connecting each flat surface, each concave edge, each convex edge, the ABC concave kink, and the ABC convex kink are individually determined using surface, first sublayer, and second sublayer H-atom sites. This results in a total of 232 rate constants (some of which are equal by symmetry and all of which are connected by detailed balance) that are included in the KMC model that simulates the H-atom mobility across and into the Ni surfaces. In Figure 1, a schematic diagram of the three surfaces A, B, and C and their surface interconnections presents the logical pattern used in the KMC simulations with boundary conditions noted at the convex (cx) and concave (cc) intersections (two layers of subsurface sites are also included in the KMC simulation which are not noted explicitly in Figure 1). The logical model in Figure 1 is not intended to represent a physical nanocrystal in 3-d space, but is instead constructed to display the competition of H-atom occupied sites among the specific atomically flat surfaces with the convex and concave interfaces noted. However, within this model, are atomically correct interfaces of the flat terrace surfaces built into the KMC simulation. For example, an atomic-model representation of one component of the schematic diagram, using a 4 × 4 site (100) surface as the point of reference, is denoted in Figure 2. This figure shows the convex step-down edges along with the convex corner pointing out toward the viewer toward the front of Figure 2; and this convex corner corresponds to the lower left corner of the (100) labeled region of Figure 1. The concave step-up edges and the concave corner in Figure 2 point away from the viewer; and this concave corner corresponds to the upper right corner of the (100) labeled region of Figure 1.

(b) Potential Energy and Rate Constants. The interaction energy used for modeling the system is the embedded-atom
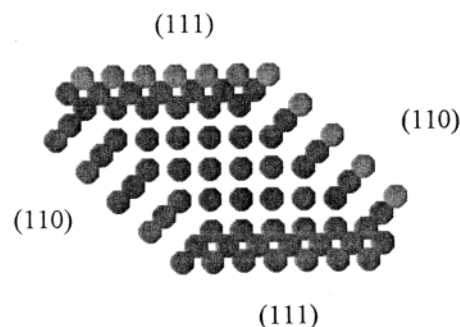

Figure 2. Sample physical-model representation of one component of the schematic diagram shown in Figure 1, using a 4 × 4 site (100) surface as the point of reference. The convex step-down edges and the convex corner are pointed out toward the viewer and the concave step-up edges away from the viewer with the (110) and (111) faces labeled.

method (EAM) potential energy proposed by Daw and Baskes[47] as modified by Wonchoba, Hu and Truhlar[48a] and we used the model which they designate as EAM5. This potential is realistic in the sense that it has been parametrized to fit the Ni−Ni equilibrium distance (with a lattice constant of 3.521 Å), and the H−Ni equilibrium distance, the surface binding energy, and hydrogen vibrational frequency for the Ni(100) surface. This potential energy surface also gives reasonable barrier heights for the H and Ni diffusion on Ni(100).[1,48a] The results of this potential for H on the (110) and (111) surfaces and in bulk Ni, while not as well represented as they are for the (100) surface are typically, but not always, in qualitative agreement with the experimental results which have been reviewed by Wonchoba and Truhlar.[48b] For example the binding energies of H on the (100) and the (110) surfaces and in the bulk Ni, values for which we report for our simulations in Table 1 using our zero point energy estimate (−2.69, −2.70, and −2.23 eV, respectively) are in reasonable qualitative agreement with experiment (approximately −2.80, −2.81, and −2.30 eV respectively[48b]) resulting in experimentally reasonable population distributions at equilibrium for these sites. However, the EAM5 potential does not agree as well with experimental results on the Ni-(111) surface. Wonchoba and Truhlar[48b] have also proposed modifications to the EAM5 potential which account for some of the discrepancy, but the modification does still not correct fully for the one key difference: the binding energy for H on (111) surface, at about −2.58 eV for the model, is estimated to be −2.87 eV experimentally. The model value is significantly different for the binding energy on the (111) surface as compared to the binding energies for the (110) and (100) surfaces that the resulting population distributions for H will diverge between theory and experiment. A similar result for the binding energy of H on the Ni(111) surface in over a half-dozen theoretical efforts (summarized by Wonchoba and Truhlar[48b]) have found a similar divergence with experiment. It has been suggested that the difference between theory and experiment for the (111) case may be related to coverage dependence effects, as the experimental results are determined at coverages of about 0.3 ML of hydrogen and site-to-site interactions are expected to be especially significant on the this surface due to its tight geometry. In very recent theoretical work, Mavrikakis[49] has carried out DFT calculations for H/Ni(111) at 0.25 ML hydrogen coverage and found a binding energy (without zero point energy, ZPE, which can typically be on the order of 0.1 eV) of −2.89 eV in very good agreement with the experimental results at similar coverages. Mavrikakis also reports a subsurface binding energy for H/Ni(111) of −2.18 eV which is in line with our value of −2.28 eV (where our value includes a ZPE estimate).

Kinetic Monte Carlo Study

J. Phys. Chem. B, Vol. 107, No. 41, 2003 **11435**

TABLE 1. Binding Energies, in eV, for the Hydrogen Top Surface and First Layer Subsurface Binding Sites for Various Ni Surfaces and Edges and the Activation Energy Barrier, in eV, for the Top to Subsurface Path

site label	site description	top site (eV)	subsurf site (eV)	top → subsurf barrier (eV)
A	surface A, the (100) surface	−2.6985	−2.2872	0.65
Ab	A/AB convex edge	−2.7014	−2.2856	0.5844
Ac	A/AC convex edge	−2.6992	−2.3035	0.565
Abc	A/ABC convex corner	−2.7061	−2.3042	0.5559
B	surface B, the (110) surface	−2.7014	−2.3060	0.55
Ba	B/AB convex edge	−2.6986	−2.2856	0.464
Bc	B/BC convex edge	−2.7002	−2.3257	0.4715
Bac	B/ABC convex corner	−2.7020	−2.3042	0.4978
C	surface C, the (111) surface	−2.5864	−2.2897	0.54
Ca	C/AC convex edge	−2.5804	−2.3035	0.4419
Cb	C/BC convex edge	−2.5922	−2.3257	0.3515
Cab	C/ABC convex corner	−2.5991	−2.3042	0.3379
D	AB (100/110) concave edge	−2.7374	−2.2718	0.7276
E	BC (110/111) concave edge	−2.5893	−2.2978	0.5925
F	AC (100/111) concave edge	−2.7166	−2.2672	0.7950
G	ABC (100/110/111) concave corner	−2.7394	−2.2409	0.7585

[a] All Bulk Ni sites, representing the second subsurface layer, are set to $E = -2.2378$ eV.

The activation barrier estimate Mavrikakis gives from the surface to the subsurface, 0.88 eV, is qualitatively similar to our value, 0.54 eV (which again includes a ZPE estimate). A comparison of these various activation energies and binding energies suggsts that the key distinction among all of these cases in regards to the KMC simulation results that we report below is the H/Ni(111) binding energy. The full effect of coverage dependence for H on this surface, to the best of our knowledge, remains unresolved and we have used the EAM5 potential for the KMC simulations reported here, with the important proviso that the results, which we believe to be very accurate within the model used, may not accurately reflect the Ni(111) surface especially. Our motivation for using the EAM5 potential rather than the EAM6 is that the H-atom distributions across the (100) and (110) surfaces are in good agreement with experiment as noted above, and these two Ni surfaces were the main focus of our previous studies on the effect of H as an impurity during epitaxial Ni growth.[4]

The binding site energies for H and the activation energies for site-to-site H mobility are calculated using this potential energy surface as described in detail in our previous work.[3] In Table 1, we note the calculated binding energies used in our KMC model for surface and subsurface sites. The bulk binding site is calculated in the same manner as in ref 3, but using six layers of Ni on all sides of the H atom (and the energies are converged with respect to adding more layers of Ni at the accuracy noted in Table 1). Note from Table 1 that among the three perfect surfaces, the (110) surface has a deepest binding energy, and the (100) surface is deeper than the (111) surface. At a temperature of 400 K (used in some of the KMC simulation below), this gives Boltzmann distribution populations of 0.470, 0.512, and 0.018 on the (100), (110), and (111) surfaces, respectively. At a temperature of 1000 K (also used in some of the KMC simulations), populations become 0.434, 0.448, and 0.118, respectively. Note also from Table 1 that some concave edge sites (those listed as sites D, F, G) generally have deeper binding energies than their adjoining flat terrace surface site energies, and that the convex edge sites have binding energies roughly in line with the adjoining flat terrace site energies. Also noted in Table 1 is that the subsurface sites are less stable energetically using the EAM5 potential. The bulk site energy is noted as a footnote to Table 1, and it has a slightly lower binding energy than the first-layer subsurface sites. These binding energy values are consistent with some of the experimental work for hydrogen: while some metal systems show penetration of hydrogen to the bulk,[50-53] in other cases an initial partial deposition of hydrogen can continue on the surface indicating that some of the H will tend to either bind to the surface or bubble to the surface during metal deposition.[1,31-35,42,43]

The hopping of an adsorbed H from one binding site to another nearest neighbor site on the Ni(100), Ni(110), and Ni(111) surfaces at the temperatures examined here is assumed to be a rare event governed by an activation energy. We determine estimated H-hopping rate constants from a simplified TST model based on the site-to-site activation energies, E_{act}. The TST model gives the rate constant estimate as

$$k = (k_B T/h)(Q^{\#}/Q) \exp(-E_{act}/k_B T) \approx$$
$$(k_B T/h) \exp(-E_{act}/k_B T) \quad (1)$$

where k_B is Boltzmann's constant, T is the temperature, h is Planck's constant, and Q ($Q^{\#}$) is the vibrational partition function of the reactant (transition state) configuration. The vibrational partition function ratio ($Q^{\#}/Q$), for H hopping has been tested for a variety of events and it is typically on the order of unity; and we set it equal to unity in the study discussed here.[1-3] The rate constant in eq 1 can be converted into a time constant, τ, assigned to a particular activated hopping event by inverting the rate constant determined from eq 1 as

$$\tau = 1/k = (h/k_B T) \exp(+E_{act}/k_B T) \quad (2)$$

To test some of the noted assumptions underlying eqs 1 and 2 and to convince ourselves that reasonable time-scales for H mobility are given within our model, we have calculated quantum mechanical rate constants for the H-hopping for several cases using the flux−flux correlation function methods as described in detail by Haug and Metiu.[54] The quantum model uses a 3-d quantum calculation for the H-atom coordinates within a mean field potential given by the relaxed Ni atom positions. Details are given in Appendix A, in which we show that the simple model of eqs 1 and 2 does indeed give reasonable orders of magnitude for the time scales for the H hopping events.

In Table 1 and in Table 2, some of the principal activation energies are noted for the H-atom surface crossing and surface penetration events. In the right-hand column of Table 1, the lowest energy barriers for direct hopping from the indicated surface top-site to corresponding subsurface site are noted. The H-atom mobilities across the flat terraces have been discussed in our previous work,[3-4] and we note here that the barriers for H-hopping on (100) is 0.17 eV, on (110) is 0.18 eV along the short-axis and 0.02 eV along the long-axis direction, and on

TABLE 2. Selected Forward Energy Barriers (in eV) for Surface Crossing, Using the Site-to-site Descriptive Labels Noted in Table 1[a]

site-to-site description	barriers (in eV)	
	forward	reverse
surface site A → B at convex edge	0.174	0.1712
surface site A → C at convex edge	0.1998	0.081
surface site B → C at convex edge	0.196	0.088
surface site A → D at concave edge	0.150	0.1889
surface site B → D at concave edge	0.027	0.063
surface site B → E at concave edge	0.189	0.0769
surface site C → E at concave edge	0.0201	0.023
surface site A → F at concave edge	0.166	0.1841
surface site C → F at concave edge	0.0328	0.163
subsurf site Ab → A	0.2584	0.260
subsurf site Ba → B	0.2596	0.280
subsurf site Bc → B	0.4497	0.43
subsurf site Cb → C	0.236	0.20
subsurf site Ac → A	0.2763	0.26
subsurf site Ca → C	0.2138	0.20

[a] All barriers are consistent with detailed balance from the site energies given in Table 1, which is why some are given to more significant figures than others.

the (111) surface is 0.02 eV from fcc-to-fcc site. Therefore while the H atoms are very mobile across all of the surfaces—the hopping time scale from eq 2 at 500 K for the 0.18 eV barrier is 3.1×10^{-12}s—the H atoms are especially adept at fleeing the low-binding energy (111) surface which affords the lowest penetration barriers. Notice that all of the surface penetration barriers are large in comparison to the terrace hopping barriers, indicating the great relative fluidity of the H atoms across the surface top. Notice also that flat terrace-site penetration barriers have higher barriers than do the convex edge sites (and that the concave sites have higher barriers still). Therefore the convex sites are expected to be important for subsurface penetration, although the reverse barriers which are given by detailed balance are also very low for these convex sites, and the kinetic modeling discussed below is needed to fully verify the H-atom flow. Table 2 also gives the energy barriers for the convex and concave crossing sites for the three surfaces of interest on both the surface top sites and the first subsurface layer sites. Note that the A−B (or 100−110) surface interchange in the first row of Table 2 is roughly symmetric with energies around 0.17 eV, but that the A−C and B−C crossing barriers are not symmetric (indicated in rows 2 and 3 and as required by the detailed balance restriction). Therefore the H atoms on the (111) surface can move off of the surface with reasonable ease at the convex edge. At the concave edge, we find similar hopping mobilities as indicated in rows 4−9 of Table 2. So in conclusion there are not any notable bottlenecks to surface crossing events for H atoms. Surface crossing mobilities for the convex edge in the first subsurface layer are also given in rows 10−15 of Table 2. Barriers in the 0.21−0.27 eV range are the norm here. Deeper layer mobilities are all modeled as bulk site-to-site mobilities with activation energies of 0.43 eV.

(c) Kinetic Monte Carlo Simulation. The kinetic Monte Carlo (KMC) method is a stochastic solution of the master equation,[55] which in our case governs the diffusion and penetration processes occurring in this system. It is based upon the assumption that the hopping events are random which is quite reasonable for most of the hopping rates of interest here, as noted above. We follow a KMC procedure similar to that discussed in more detail for Ni mobility on Ni surfaces in Haug and Jamoury.[4] In our present work, the H atoms are initiated on a terrace surface site representing an infinitely dilute coverage (noninteracting H atoms). The H atoms then are moved from

site-to-site with probabilities for a move proportional to the appropriate rate constant, with the probability for a hop (P_i) given by $P_i = k_i/k_{ref}$, where k_i is the rate constant for event "i" which refers to a given Ni hopping event and k_{ref} is taken to be the rate constant corresponding to a reference event which sets the clock cycle. In our case k_{ref} is chosen via eq 2 to represent a time constant $\tau = 4.6 \times 10^{-16}$ s at $T = 1000$ K as the simulation clock-cycle, which is 2 orders of magnitude smaller than the faster hopping event. This 2 order of magnitude time separation was needed to accurately track the transient H-atom kinetics happening at the surfaces on the pathway to an equilibrium distribution. Several hundred (typically 900) independent H atoms are followed to give reasonable statistical average pathways discussed in section III below. Forward and reverse rates connect all possible hops, and are consistent with the binding site energies so that detailed balance is preserved. Therefore with enough time the statistical Boltzmann probabilities for occupancy of various sites is ensured and can be seen developing in the discussion and figures in section III.

The KMC results reported here involve the boundary conditions indicated in Figure 1 so that if any atom leaves one surface it will appear on the connected surface. The simulations discussed here use three layers in the surface perpendicular direction (surface site, subsurface site, and second layer subsurface site, which is assumed to be a bulk subsurface site energetically). The key observables of interest are the time scales for site populations and the pathways to equilibrium for the H atoms. We examine several temperatures but use only one standard surface size and that implies one characteristic roughness in terms of the relative number of kink-sites. In the work reported below, we use A, B, and C surfaces that are each 10 × 10 in site numbers, giving a roughness measure of 18% of total surface sites being surface edge sites. The significant number of edge sites better illuminates the roughness effects on a shorter KMC time scale as an aid in the computational effort. In the patterns that we report below, surface roughness does turn out to be an important factor (in comparing the infinitely flat surfaces with our fixed roughness interacting surfaces which are 10 × 10 sites each) as the convex kink sites are important for surface penetration. However, as expected, these factors scale directly with the relative number of such edge sites, and test calculations at different roughness levels have not illuminated any significantly different features to warrant including them here. Also, in this set of studies we do not report on adjusting for H-atom coverage, in which an H atom at one site would block the occupancy of another H atom. However, in test calculations we have found no significant differences in the noninteracting H-atom model reported here with coverage-dependent models, at least when the H-atom initial surface coverage is less than about 0.10 ML.

III. KMC Results

In our report of the results of the KMC simulations, our focus is an examination of the pathways and time scales for the H atom population being distributed across the faceted surface and into the immediate subsurface layer. We have carried out calculations at temperatures from 400 to 1000 K, in which the higher temperatures are not so much of experimental interest but do speed the dynamics of the calculations and therefore improve upon the statistical accuracy of our KMC results. The temperature variation also allows us to examine the closing of certain pathways into the subsurface as the temperature decreases.

To show the general nature of the deposited H population approach to equilibrium upon and into the connecting Ni
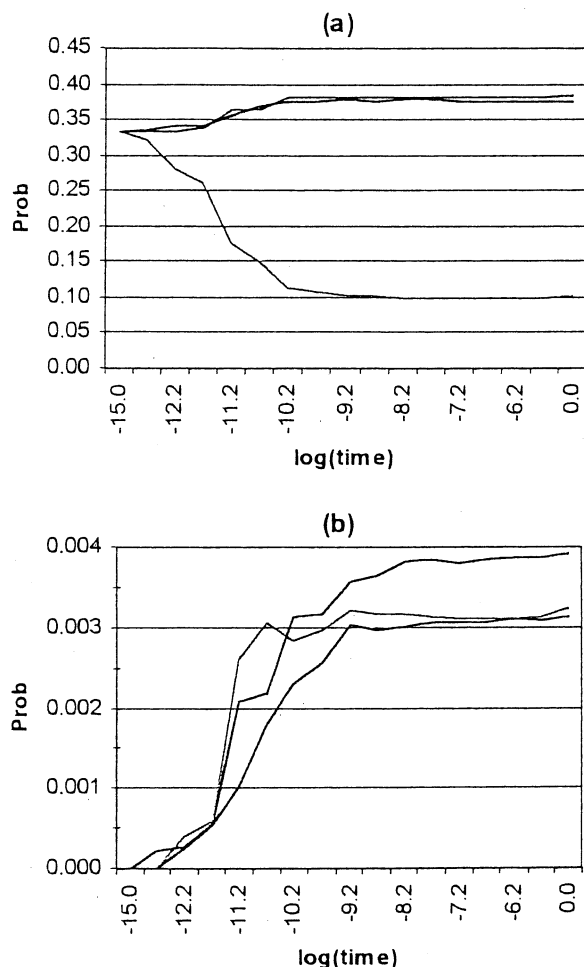
Kinetic Monte Carlo Study

J. Phys. Chem. B, Vol. 107, No. 41, 2003 **11437**

Figure 3. Probability distributions for H atom populations as a function of time (in seconds, on a log scale) evolving at 1000 K from initial values of 0.333 on the surface of each (100), (110), and (111). The right-hand end point of each curve is the Boltzmann statistical distribution for the H atoms for our sample system. Part a shows the surface probabilities evolving, with curves from top to bottom denoting (110), (100), and (111) respectively on the right side of the figure. Part b shows the first subsurface layer probabilities evolving, with curves from top to bottom denoting (110), (111), and (100) respectively on the right side of the figure.

surfaces, we begin with the $T = 1000$ K example. On connected, but otherwise flat surfaces, the H atom populations are initially distributed across the top of the surface. General features of the kinetic pathways taken to equilibrium are seen in Figure 3 in which equal ($^1/_3$) population fractions of H atoms are initiated on each of the (100), (110), and (111) surfaces, as seen on the left-hand axis of Figure 3a. The H atoms then flee the (111) surface, the lower curve in Figure 3a, to the other two surfaces and also penetrate slightly into the subsurface layers of all three surfaces. The time scale for surface and subsurface equilibrium is about 10^{-9}–10^{-8} s for the 18% roughness test case seen in Figure 3. This equilibrium time will clearly depend on the roughness of the surface, but rather weakly unless very large surface domains are used due to the rapid surface hopping which occurs with a time scale on the order of 10^{-13} seconds or faster on the three surfaces. On the far right side of Figure 3a, the last data point is the Boltzmann statistical distribution for the H atoms on each surface in our sample system. In part b of Figure 3, the (100), (110), and (111) first layer subsurface populations are indicated as they evolve from zero probabilities, and again on the far right side of the figure the last data point is the Boltzmann statistical distribution for the H atoms. More
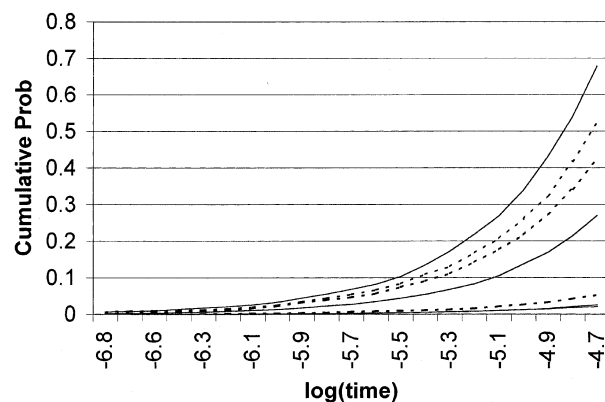

Figure 4. Cumulative probability for pathways to reach the first sublayer as a function of time (in seconds, on a log scale) at 500 K. The three dashed curves in Figure 4 correspond to the unconnected surface model in which dashed curves from top to bottom denote the (111), (110), and (100) surface penetration pathways, respectively. The four solid curves in Figure 4 correspond to the connected surface model in which solid curves from top to bottom denote the convex edge pathway, the (110), (111) and (100) surface penetration pathways. Note that the (111) and (100) surface pathways are essentially on top of each other.

Monte Carlo noise arises in Figure 3b due to the low probabilities involved, but clearly the equilibrium sublayer population is being achieved by about 10^{-9} s at this temperature.

The dynamic pathways into the subsurface involve both direct terrace site penetration and especially convex edge site penetration, the balance between the pathways depending on temperature. The major effect of lowering the temperature in our model from 1000 to 500 to 400 K is to essentially rescale the time to equilibrium, but of course some of the pathways to the subsurface are also being closed down depending on their activation energies. We will first examine the pathways to the subsurface for the 500 K case in more detail, and then we will examine the temperature dependence of the pathways. In Figure 4, we compare the set of connected surfaces with the infinite separate surfaces (zero % roughness), and we plot the cumulative probability for reaching the first sublayer. The pathways shown are via either direct penetration of the terrace surfaces (A, B, and C), or alternately for the connected surface via convex edge site penetration. The three dashed curves in Figure 4 correspond to the infinite-size, separate surfaces in which direct surface penetration is the only pathway. The top dashed curve rising to a value of about 0.52 represents the C (111) surface, the middle dashed curve rising to 0.43 is the B (110) surface, and the lower dashed curve rising to 0.05 is the A (100) surface, and together their final cumulative probabilities add to unity. The ordering among these surfaces is as expected from the energy barriers in Table 1. The solid curves in Figure 4 correspond to the connected surface model in which direct terrace penetration is still occurring, but is now supplemented by concave and convex site penetration as well. In particular, the convex sites allow a significant flux of atoms to the subsurface. The top solid curve, rising to a value of about 0.68, represents the cumulative probability for reaching the subsurface via all of the convex edges. The middle solid curve, rising to a value of about 0.27, represents direct terrace penetration for the B (110) surface, and the lower solid lines (there are two essentially on top of each other which rise to a value of about 0.02) are for direct terrace penetration for the C (111) and the A (100) surfaces. The key feature for the connected surfaces is the convex edge pathway to the subsurface. The 68% probability for H atoms moving to the subsurface at the convex edges, in itself has contributions

11438 *J. Phys. Chem. B, Vol. 107, No. 41, 2003*

Haug and Raibeck

TABLE 3. Percentage of H Atoms Leaving Each Surface Across the Concave and Convex Step-Edge Pathways for the 500 K Connected Surface Case

initial surface	toward final surface	pathway: edge type	% of total
(100)	(110)	convex	27.7
	(111)	convex	14.5
	(110)	concave	33.9
	(111)	concave	23.8
(110)	(100)	convex	4.0
	(111)	convex	2.3
	(100)	concave	91.5
	(111)	concave	2.1
(111)	(100)	convex	12.0
	(110)	convex	13.5
	(100)	concave	42.6
	(110)	concave	31.9

of 38% via the (110)/(111) convex edge, 21% via the (100)/(110) convex edge, 3.5% via the (100)/(111) edge, and 5.5% via the (100)/(110)/(111) convex corner. The importance of the (110) convex edges result from the tradeoff seen in Table 1 of reasonably low penetration barriers with stable top-surface sites, and the importance of the (111) edge is due to the atoms fleeing that surface across the convex edge coupled with the low barrier to penetrate especially at the (111/110) convex step edge. Note also the relative importance of the convex corner—the number of edge sites is an order of magnitude greater than that of the corner itself.

The pattern of subsurface pathways is somewhat affected by temperature. In Figure 5a–c, we examine the temperature dependence of the cumulative probability for reaching the first sublayer as a function of time for $T = 400, 500,$ and 1000 K, respectively. The top curves in each part of Figure 5a–c follow the same general pattern as the solid curves in Figure 4. The top curve is the cumulative probability for reaching the subsurface via all of the convex edges, the middle solid curve, is direct terrace penetration for the B (110) surface, and the lower curves (there are two on top of each other) are for direct terrace penetration for the C (111) and the A (100) surfaces. Two points to note are the time scale differences, which again is indicative of the speed-up of dynamics with temperature, and the change in cumulative probabilities especially at 1000 K (also notice in Figure 5c that the probability scale differs). In the 1000 K case, the barriers to penetration of the terrace are becoming less significant and the convex edge penetration curve just barely rises above the (110) penetration curve. Note also that the (100) and (111) direct penetration curves are also becoming competitive at this temperature. A comparison to the 400 and 500 K cases illustrates the closing of the terrace penetration pathway as temperature falls until at 400 K about 78% of all subsurface atoms over 10^{-4} s are finding there way to the subsurface via the convex edge sites.

In conjunction with surface penetration is the surface crossing pattern, which is summarized for the 500 K case in Table 3. In that table, we note the percentage of top-to-top surface crossings from each of the three surfaces (listed as initial surface) to final surfaces via either the convex or concave step edges. The percentages for each group add to 100. Note that for the (100) and the (111) surfaces, significant exit paths exist across all four borders with differences due to the activation barriers and binding sites at the edges. The concave edges have more stable binding sites (seen in Table 1) and draw H-atoms into them which appears in the higher percentages for concave edges in Table 3. The (110) case is distinctly different due to the asymmetry of hopping barriers for H-atom mobility along the short vs long axis as noted above and discussed more extensively
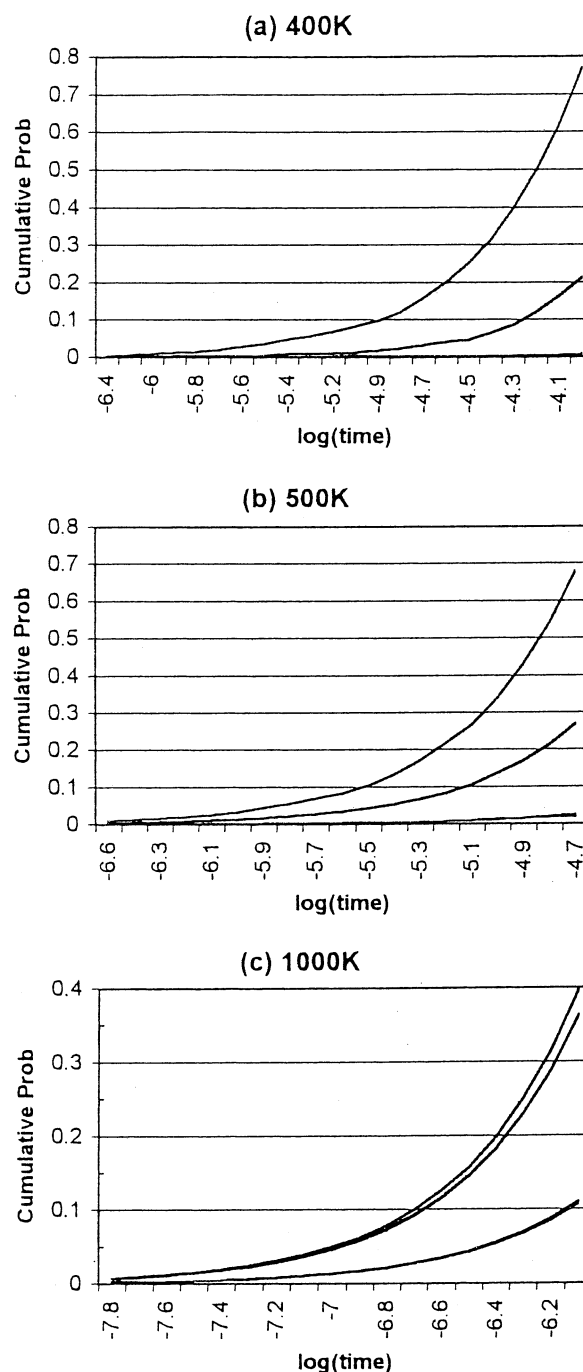

Figure 5. Cumulative probability for pathways to reach the first sublayer as a function of time (in seconds, on a log scale) for the connected surface models at (a) 400, (b) 500, and (c) 1000 K. The four solid curves in each part from top to bottom denote the convex edge pathway, the (110), (111) and (100) surface penetration pathways. Note that the (111) and (100) surface pathways are essentially on top of each other in each case.

in ref 3 and 4. Preferential interchange occurs with the (100) surface since the (111) surface intersects with (110) via the more restricted direction.

The importance of the convex edge in surface penetration suggests that a circulating hydrogen current will flow from an initial nonequilibrium distribution of surface H atoms until the equilibrium distribution is reached. This circulating pattern can be anticipated by noting the subsurface activation energies for moving back from the convex step edge, indicated in the second column of rows 10–15 in Table 2. These barriers are typically on the order of 0.25 eV vs the direct terrace penetration barriers
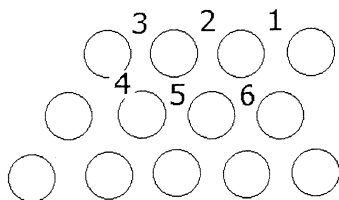
Kinetic Monte Carlo Study

J. Phys. Chem. B, Vol. 107, No. 41, 2003 **11439**

Figure 6. Schematic diagram indicating the 6 states used in the continuum kinetics model. More extended models have also been examined coupling sites on both sides of the convex edge for example and give very similar results. Sites 1−3 are surface (111) states, with site 3 being the convex step edge adjoining the (110) surface; site 4 is the convex edge subsurface site, and sites 5 and 6 are (111) sublayer sites.

of 0.54 eV or more (given in Table 1). With sublayer H atoms then under the terrace, they can in turn bubble back up to the surface layer, move back to the step edge, and loop around again. As long as a nonequilibrium pressure is maintained to drive the current it continues, but weakens as a few atoms are lost to equilibrium in each cycle, and the eddy eventually dies. We can track this circulating H current in the KMC studies, but it is easiest to illustrate with a simple classical kinetic model that we describe next.

IV. Hydrogen Current Model

Hydrogen atoms deposited on our model Ni surfaces are in a nonequilibrium distribution—having a low, but definite, probability to be found in the first sublayer as well as deeper bulk layers of the Ni. The H atoms also show a preference to penetrate the surface at convex step edges rather than throughout the terrace. Once in the first subsurface layer the Hydrogen can migrate back under the flat terrace, from which it readily bubbles back to the top terrace. The net pathway represents a cyclic current, an eddy in the H-atom probability river, which continues until the equilibrium distribution of H is reached. To illustrate this more clearly we use a six-state continuum kinetics model representing a two-dimensional crosscut of the Ni surface at a step edge as displayed in Figure 6. More extended models have also been examined coupling sites on both sides of the convex edge for example and give very similar results. In Figure 6, sites 1−3 are on the top (we use the 111) surface, with site 3 being the convex step edge (we use the 111/110 edge), and sites 2 and 1 moving back away from the edge. Site 4 is the convex edge subsurface site, and sites 5 and 6 are (111) sublayer sites moving back away from the convex edge. The same energies and barriers are used for these sites that are used in the full KMC model. The simple model begins with equal ($^1/_3$) probabilities being initiated at sites 1−3 with the dynamics following standard classical chemical kinetics:

$$dN_j/dt = (\Sigma_i \, k_{i-j} N_i) - (N_j \, \Sigma_i \, k_{j-i})$$

where $\{N_j\}$ labels population fractions at sites 1−6, and k_{i-j} is the rate constant for transition from site $i \rightarrow j$. Details of the computational techniques used are given by Haug and Truhlar.[56] The H-atom probability current is measured by examining the counterclockwise flux from sites (2−3−4−5−2) minus the clockwise flux of the same sites. If sites 1−3 are all equivalent, and 4−6 are all equivalent, then of course no net current results. But since the edge sites (3 on the surface and 4 in the subsurface) have slightly different energies and entrance/exit barriers, as noted in Table 1, then the eddy of flux develops during the transient time until equilibrium probabilities are reached. Total energy conservation and detailed balance are maintained
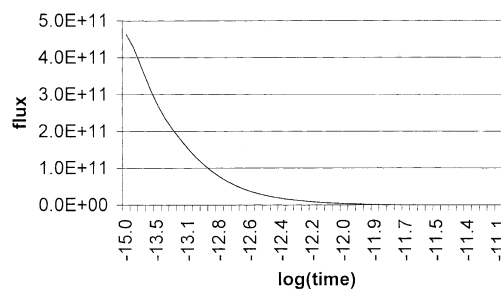

Figure 7. H-atom net flux of probability current measured by examining the counterclockwise flux from sites (2−3−4−5−2) of Figure 6 minus the clockwise flux of the same sites plotted as a function of time (in seconds, on a log scale). The temperature is 1000 K.

throughout the model. The eddy of flux is displayed in Figure 7 for a temperature of 1000 K where we see the net counterclockwise flux dominating over the $10^{-15}-10^{-13}$s time range and dying off by about 10^{-12} s. Equilibrium is reached more quickly in the simple model than in the full KMC since the pathways are so limited in the model.

V. Summary

We examine H-atom pathways across a model of connected Ni (100), (110), and (111) surfaces, and also the pathways into the subsurface layers of these surfaces. Our interest is in finding the time scale for an initial H-atom population density deposited on the surface to reach an equilibrium surface and sublayer distribution, and to understand the H dynamics in the region of Ni surface steps. This understanding in turn will help in our understanding of the stability of the Ni step edge, since sublayer H atoms have been found to significantly affect the Ni mobility.[4] A realistic set of 232 simplified transition state rate constants governs the H-hopping model, which in turn is based on an embedded atom model of the potential energy function (borrowed from the literature). A handful of these simplified rate constants are compared favorably to very accurate calculations of rate constants for the same potential using a 3-d quantum mean field method (discussed in Appendix A). With this set of rate constants, KMC simulations of noninteracting H-atom mobility are carried out for several temperatures. We note the time scale for the approach to equilibrium for the H-atoms on both the surfaces and subsurfaces which is summarized in Figure 3. In Figures 4 and 5, the effect of convex step edges vs the effect of direct terrace penetration for the H atoms is examined. We find that, at temperatures below about 1000 K, the H-atom penetration at convex step edges and corners becomes the favored pathway to the subsurface. As the H atoms flow via the step edges to the sublayer, a transient cycling current is set up near the step edge, which fades away as equilibrium is reached, summarized in the kinetic model of Figures 6 and 7.

Appendix A

In this appendix, we report on calculations of quantum mechanical rate constants for the H-hopping for several cases from our model and compare them to the simplified TST value of the rate constant. For the quantum model we use the flux−flux correlation function methods described in detail by Haug and Metiu.[54] The Ni surface is treated with a two-term classical mean field method—using relaxed Ni positions for the H atom

TABLE 4. Comparison of Escape Rate Constants at 400 K for Quantum Flux−Flux Correlation Calculation Using the Quantum Mean Field Model (qmf) vs the Transition State Approximation Model for Selected Surface Hop Transitions

transition	energy barrier (eV)		rate constant (fs^{-1})	
	qmf	model	k(qmf)	k(model)
(100) surface hop	0.173	0.170	5.24(−5)	8.71(−6)
(110) long-axis surface hop	0.17889	0.18	2.94(−6)	6.16(−6)
(110) short-axis surface hop	0.03709	0.0323	3.02(−3)	1.79(−3)
(111) surface hop	0.03476	0.023	2.42(−3)	2.57(−3)
bulk Ni site-to-site hop	0.4205	0.43	7.30(−10)	3.73(−10)

at the equilibrium binding site and using the relaxed Ni positions for the H atom at the transition state site. The H-atom's three coordinates are treated by a fully quantum calculation, giving the rate constant for binding site escape for site "i" to site "f" as

$$k_q(\text{i}\rightarrow\text{f}) = (1/Q_r) \int_o^\infty C_{ff}(t)\,dt =$$
$$(C_{ff}(0)/Q_r) \int_o^\infty [C_{ff}(t)/C_{ff}(0)]\,dt \quad (A1)$$

The partition function for the reactant configuration, Q_r, is determined from the equilibrium mean field calculation and the correlation function, $C_{ff}(t)$ from time zero to a convergence time, is determined from the transition state mean field. For a meaningful rate constant, the integral of the time-dependent kinetic factor must converge on a time scale consistent with the loss of activation to the surface (if the surface were dynamic). From the calculations of Zhang, Haug, and Metiu[57] this time scale is on the order of about 100 fs for H on a similar Ni potential energy surface. We find convergence of the integrals for our sample calculations at around 40fs indicating that the rate constant values given by eq A1 should be quite accurate. Table 4 compares the rate constants using eq A1 to the approximate TST theory of eq 1 for the cases indicated. Note that good order of magnitude predictions are given by the TST theory, which is all that we could expect. Note also that some of the very low energy barriers noted in the text, such as the H-hopping across the (111) surface with a barrier energy of around 0.02 eV (and therefore a time constant in the hopping model of about 1.5×10^{-13} s or 150 fs at 500 K) are probably only borderline accurate as represented by the simple TST result of eq 1.

References and Notes

(1) Haug, K.; Zhang, Z.; John, D.; Walters, C. F.; Zehner, D. M.; Plummer, W. E. *Phys. Rev. B*. **1997,** *55*, R10233−R10236.

(2) Haug, K.; Do, N. K. N. *Phys. Rev. B*. **1999,** *60*, 11095.

(3) Haug, K.; Jenkins, T. *J. Phys. Chem. B*. **2000,** *104*, 10017.

(4) Haug, K.; Jamoury, *J. Phys. Chem. B*. **2002,** *106*, 11253.

(5) Trevor, D. J.; Chidsey, C. E. D. *J. Vac. Sci. Technol. B* **1991,** *9*, 964.

(6) De la Figuera, J.; Pristo, J. E.; Ocal, O.; Miranda, R. *Solid State Commun*. **1994,** *89*, 815.

(7) Morgenstern, K.; Rosenfeld, G.; Poelsema, B.; Comsa, G. *Phys. Rev. Lett*. **1995,** *74*, 2058.

(8) Wen, J.-M.; Chang, S.-L.; Burnett, J. W.; Evans, J. W.; Thiel, P. A. *Phys. Rev. Lett*. **1994,** *73*, 2591.

(9) Hamilton, J. C.; Daw, M. S.; Foiles, S. M. *Phys. Rev. Lett*. **1995,** *74*, 2760.

(10) Van Siclen, C. DeW. *Phys. Rev. Lett*. **1995,** *75*, 1574.

(11) Khare, S. V.; Bartelt, N. C.; Einstein, T. L. *Phys. Rev. Lett*. **1995,** *75*, 2148.

(12) Sholl, D. S.; Skodje, R. T. *Phys. Rev. Lett*. **1995,** *75*, 3158.

(13) Voter, A. F. *Phys. Rev. B* **1986,** *34*, 6819.

(14) Stumpf, R. *Phys. Rev. Lett*. **1997,** *78*, 4454.

(15) Kellogg, G. L. *Phys. Rev. B*. **1997,** *55*, 7206.

(16) More, S.; Berndt, W.; Bradshaw, A. M.; Stumpf, R. *Phys. Rev. B*. **1998,** *57*, 9246.

(17) Khare, S. V.; Einstein, T. L. *Phys. Rev. B*. **1998,** *57*, 4782.

(18) Huang, Y.-C.; Flidr, J.; Newton, T. A.; Hines, M. A. *Phys. Rev. Lett*. **1998,** *80*, 4462.

(19) Kellogg, G. L. *Phys. Rev. Lett*. **1998,** *79*, 4417.

(20) Bogicevic, A. *Phys. Rev. Lett*. **1999,** *82*, 5301.

(21) Tung, R. T.; Graham, W. R. *Surf. Sci*. **1980,** *97*, 73.

(22) Peale, D. R.; Cooper, B. H. *J. Vac. Sci. Technol. A* **1991,** *10*, 2210.

(23) Esch, S.; Hohage, M.; Michely, T.; Comsa, G. *Phys. Rev. Lett*. **1994,** *72*, 518.

(24) Vrijmoeth, J.; van der Vegt, H. A.; Meyer, J. A.; Vlieg, E.; Behm, R. J. *Phys. Rev. Lett*. **1994,** *72*, 3843.

(25) Oppo, S.; Fiorentini, V.; Scheffler; M. *Phys. Rev. Lett*. **1993,** *71*, 2437.

(26) Zhang, Z. Y.; Lagally, M. G. *Phys. Rev. Lett*. **1994,** *72*, 693.

(27) Copel, M.; Tromp, R. M. *Phys. Rev. Lett*. **1994,** *72*, 1236.

(28) Kellogg, G. L.; Plass, R. A. *Surf. Rev. Lett*. **2000,** *7* (5−6), 649.

(29) Thurmer, K.; Reutt-Robey, J. E.; Williams, E. D.; Uwaha, M.; Emundts, A.; Bonzel, H. P. *Phys. Rev. Lett*. **2001,** *87*, 186102.

(30) Montalenti, F.; Sorensen, M. R.; Voter, A. R. *Phys. Rev. Lett*. **2001,** *87*, 126101.

(31) Wortman, R.; Gomer, R.; Lundy, R. *J. Chem. Phys*. **1957,** *27*, 1099.

(32) George, S. M.; DeSantolo, A. M.; Hall, R. B. *Surf. Sci*. **1985,** *159*, L425.

(33) Mullins, D. R.; Roop, B.; Costello, S. A.; White, J. M. *Surf. Sci*. **1987,** *186*, 67.

(34) Lin, T.-S.; Gomer, R. *Surf. Sci*. **1991,** *255*, 41.

(35) Zhu, X. D.; Lee, A.; Wong, A. *Phys. Rev. Lett*. **1992,** *68*, 1862.

(36) Whaley, K. B.; Nitzan, A.; Gerber, R. B. *J. Chem. Phys*. **1986,** *84*, 5181.

(37) Auerbach, A.; Freed, K. F.; Gomer, R. *J. Chem. Phys*. **1987,** *86*, 2356.

(38) Li, Y.; Wahnstrom, G. *Phys. Rev. Lett*. **1992,** *68*, 3444.

(39) Horch, S.; Lorensen, H. T.; Helveg, S.; Laegsgaard, E.; Stensgaard, I.; Jacobsen, K. W.; Norskov, J. K.; Besenbacher, F. *Nature* **1999,** *398*, 134.

(40) Favier, F.; Walter, E. C.; Zach, M. P.; Benter, T.; Penner, R. M. *Science* **2001,** *293*, 2227.

(41) Ogasawara, H.; Brena, B.; Nordlund, D.; Nyberg, M.; Pelmen-shivkov, A.; Pettersson, L. G. M.; Nilsson, A. *Phys. Rev. Lett*. **2002,** *89*, 276102.

(42) Quattrucci, J. G.; Jackson, B.; Lemoine, D. *J. Chem. Phys*. **2003,** *118*, 2357.

(43) Go, E. P.; Thuermer, K.; Reutt-Robey, J. E. *Surf. Sci*. **1999,** *437*, 377.

(44) Kamakoti, P.; Sholl, D. *Abs. Pap. Am. Chem. Soc*. **2002,** *224*, 168. Skoulidas A. I.; Ackerman, D. M.; Johnson, J. K.; Sholl, D. S. *Phys. Rev. Lett*. **2002,** *89*, 185901.

(45) Farangis, B.; Nachimuthu, P.; Richardson, T. J.; Slack, J. L.; Perera, R. C. C.; Gullikson, E. M.; Lindle, D. W.; Rubin, M. *Phys. Rev. B*. **2003,** *67*, 85106.

(46) Tsong, T. T. In *Surface Diffusion: Atomistic and Collective Processes*; Tringides, M. C., Ed.; Plenum Press, New York, 1997.

(47) Daw, M. S.; Baskes, M. I. *Phys. Rev. B* **1984,** *29*, 6443.

(48) (a) Wonchoba, S. E.; Hu, W. H.; Truhlar, D. G. *Phys. Rev. B* **1995,** *51*, 9985. (b) Wonchoba, S. E.; Truhlar, D. G. *Phys. Rev. B* **1996,** *53*, 11222.

(49) Greeley, J.; Mavrikakis, M. *Surf. Sci*. **2003,** *540*, 215.

(50) Eberhardt, W.; Greuter, F.; Plummer, E. W. *Phys. Rev. Lett*. **1981,** *46*, 1085.

(51) Rieder, K. H.; Stocker, W. *Phys. Rev. Lett*. **1986,** *57*, 2548.

(52) Behm, R. J.; Penka, V.; Cattania, M. G.; Christman, K.; Ertl, G. *J. Chem. Phys*. **1983,** *78*, 7486.

(53) Johnson, A. D.; Maynard, K. J.; Daley, S. P.; Yang, Q. Y.; Ceyer, S. T. *Phys. Rev. Lett*. **1991,** *67*, 927.

(54) Haug, K.; Metiu, H. *J. Chem. Phys*. **1991,** *94*, 3251.

(55) Fichthorn, K. A.; Weinberg, W. H. *J. Chem. Phys*. **1991,** *95*, 1090.

(56) Haug, K.; Truhlar, D. G. *J. Phys. Chem*. **1985,** *89*, 3198.

(57) Zhang, Z.; Haug, K.; Metiu, H. *J. Chem. Phys*. **1990,** *93*, 3614.